ORIGINAL RESEARCH ARTICLE

Incipient Plasticity of a Non-equiatomic $Co_{21.5}Cr_{21.5}Fe_{21.5}Mn_{21.5}Ni_{14}$ Multi-principal Element Alloy

CHETHAN KONKATI and ANKUR CHAUHAN

To fully understand how multi-principal element alloys (MPEAs) behave when deformed, it is necessary to investigate their dislocation nucleation mechanisms or incipient plasticity and determine if they differ from pure metals and alloys. In this study, nanoindentation experiments have been performed on a non-equiatomic variant of Cantor alloy ($Co_{21.5}Cr_{21.5}Fe_{21.5}Mn_{21.5}Ni_{14}$) with low stacking fault energy. The first pop-in loads and displacements were found to be dependent on loading rates and grain orientation. The range of maximum shear stress required to cause incipient plasticity was approximately 1/13 to 1/10 of the shear modulus, indicating that the nucleation of dislocations triggered pop-in events. This was further supported by transmission electron microscopy results, which revealed a high density of dislocations under planar slip and stacking faults beneath the indent impression. The activation volume exhibits minor variation with orientation and loading rate; however, it consistently falls within the same order of magnitude, approximately equal to one atomic volume. Both homogeneous and heterogeneous dislocation nucleation mechanisms facilitated incipient plasticity. The obtained activation volume of the non-equimolar variant of Cantor alloy was higher than that of pure metals but lower than that of equiatomic CoCrFeMnNi MPEA.

Graphical Abstract

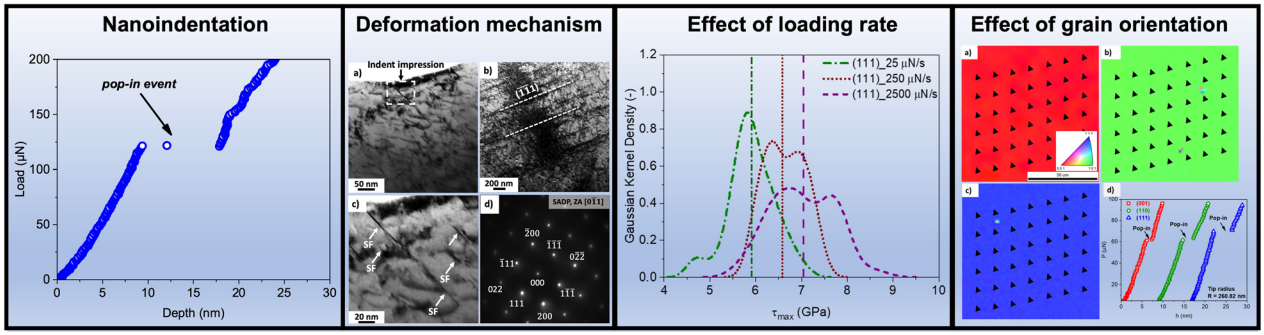

https://doi.org/10.1007/s11661-023-07146-1

I. INTRODUCTION

MULTI-PRINCIPAL element alloys (MPEAs) have gained significant attention recently due to their unique atomic structures and promising mechanical properties.[1–3] For example, a single-phase equiatomic face-centered-cubic (FCC) CoCrFeMnNi alloy exhibits a high work-hardening rate,[4–6] good ductility, and ultimate tensile strength exceeding 600 MPa at both cryogenic and room temperatures.[6–8] The alloy's high

CHETHAN KONKATI, and ANKUR CHAUHAN are with the Department of Materials Engineering, Indian Institute of Science, Bengaluru, Karnataka, 560012, India. Contact e-mail: ankurchauhan@iisc.ac.in
Manuscript submitted April 30, 2023; accepted July 16, 2023.
Article published online July 27, 2023

ductility is attributed to its relatively low stacking fault energy (SFE: 30 to 35 mJ/m^2[9,10]), which facilitates deformation twinning, while its high strength is due to the presence of different-sized atomic species and diverse local bonding environments that provide high solid solution and grain boundary strengthening.[11] Deformation mechanisms underlying the unique mechanical properties of MPEAs have been extensively explored in literature and are generally similar to those observed in conventional alloys.[2,6,12–14] However, to gain a comprehensive understanding of plasticity in MPEAs, it is crucial to investigate less explored dislocation nucleation mechanisms (incipient plasticity) in these alloys and their potential differences from that observed in pure metals and conventional alloys. This is crucial to validate the modeling work and reveal the physical origin of the high strength in MPEAs, where nucleation is the limiting process.

Nanoindentation is a widely used technique to investigate incipient plasticity, which involves bringing a sharp indenter tip into contact with the material to induce deformation at the sub-micron level.[15–19] Since the deformed volume is small, the probability of the tip encountering pre-existing defects is low.[20] Therefore, the incipient plasticity, characterized by first displacement bursts or pop-in events, is usually attributed to dislocation nucleation in the crystal. However, incipient plasticity in some cases has also been ascribed to phase transformation,[21] matrix cracking,[22] or oxide film cracking.[23–25] Additionally, Schuh *et al.*[26,27] used a combination of transition state theory and Weibull statistics in their numerical modeling to propose that pop-in behavior is a thermally activated process biased by stress. They derived relevant activation energy and volume through first-order approximation. Therefore, in general, dislocation nucleation is characterized by both athermal (*e.g.*, athermal stress) and thermal activation parameters (*e.g.*, activation energy and volume).[28,29]

Recently, efforts have been carried out both experimentally and theoretically to elucidate the dislocation nucleation mechanism in an equiatomic CoCrFeMnNi[30–32] and other MPEA systems having FCC[17,33–35] and BCC[36–38] crystal structures. Particularly for equiatomic CoCrFeMnNi, the nature of incipient plasticity is identified to proceed by heterogeneous dislocation nucleation process with vacancy-like defects (~3 atoms) as the rate-limiting nuclei. Furthermore, it has been demonstrated that the activation volume required for dislocation nucleation in equiatomic CoCrFeMnNi is much larger than that in pure FCC metals. This phenomenon has also been observed in single-phase BCC MPEAs.[36–38] The results indicate that dislocation nucleation in MPEAs involves a heterogeneous process where multiple atoms cooperatively migrate, as opposed to the conventional mechanism of direct atom-vacancy exchange, resulting in increased activation volumes.

Although previous studies have provided valuable insights, the understanding of dislocation nucleation mechanisms in MPEAs is still limited. Therefore, further investigations are required to comprehend these mechanisms further and understand composition-based differences in the MPEAs mechanical behaviors. Moreover, given that the mechanical properties of MPEAs are significantly affected by their SFE,[13,39–41] it is crucial to examine its influence on the early stages of plastic deformation (incipient plasticity). This aspect has rarely been explored, even for conventional alloys.[42] Therefore, the motivation of the present work is to determine the incipient plasticity in a non-equiatomic variant of Cantor alloy having low SFE by nanoindentation. Notably, the SFE of the CoCrFeMnNi system can be reduced by decreasing the Ni content.[39] To achieve this, the Ni content of an equiatomic CoCrFeMnNi was reduced, as it has the highest SFE (125 mJ/m^2) among the five constituent elements. This resulted in a non-equiatomic $Co_{21.5}Cr_{21.5}Fe_{21.5}Mn_{21.5}Ni_{14}$ alloy, with a low SFE of around 7.7 to 8.8 mJ/m^2, as estimated by a first-principles calculation.[39] The study also investigates the effect of loading rate and grain orientation on pop-in behavior and compares the findings with pure metals and equiatomic CoCrFeMnNi MPEA.

II. MATERIAL AND METHODS

The $Co_{21.5}Cr_{21.5}Fe_{21.5}Mn_{21.5}Ni_{14}$ MPEA was prepared by vacuum arc melting using constituent elements of ~ 99 wt pct purity in a Ti-guttered Ar gas atmosphere. The obtained ingot was remelted four times, sliced into sections of 10 × 10 × 0.8 mm^3 dimension, and thereafter homogenized for 72 hour at 1150 °C in a vacuum tubular furnace. Before microstructure characterization and indentation experiments, the sample surface was prepared carefully. The samples were firstly ground till 4000-grit silicon carbide paper. Thereafter, the sample was polished using 1 and 0.25-μm diamond suspensions and vibratory polished on Buehler's setup with a colloidal silica suspension (particle size: 0.05 μm) for 8 to 10 hours to achieve a mirror-finished surface. To remove any work-hardened surface layer prior to nanoindentation experiments, all mechanically polished samples were electropolished on Struers Lectropol equipment with A2 solution at 35 V for 13 seconds at a flow rate of 17.

A Rigaku Smartlab X-ray diffractometer with copper source (Cu–Kα radiation, λ = 0.154 nm) was employed for the phase and texture analysis. X-ray diffraction (XRD) pattern was acquired using the following parameters: 2θ-range from 20 deg to 110 deg, the scan rate of 2.2 deg/min, step size $\Delta 2\theta$ = 0.006 deg and an integration time of 280 seconds. Electron backscattered diffraction (EBSD) analysis was performed on Carl Zeiss Gemini 450 field emission-based scanning electron microscope equipped with an EDAX detector to identify grains orientation. The EBSD data were acquired at an accelerating voltage of 25 kV, 13 nA probe current, and a step size of 3 μm. The acquired EBSD data were processed and analyzed using EDAX's OIM software (version 8.0).

Transmission electron microscopy (TEM) was employed to verify that the as-homogenized material is single-phase FCC and to check for any defects and

segregation beneath the sample surface. Additionally, investigations were also carried out beneath the indent impression to characterize deformed microstructure. These investigations were conducted using a high-resolution FEI Tecnai T20 microscope operating at 200 kV, which was equipped with a Gatan double-tilt holder. The TEM lamellae were prepared using an FEI Scios focused-ion beam (FIB) scanning electron microscope (SEM). TEM lamellae were extracted out beneath the electropolished sample surface and nanoindent impression. Upon lift-out, the lamellae were attached to the molybdenum TEM half-grid by Pt deposition. Finally, the lamellae were thinned down to electron transparency (to a thickness of ~ 80 nm) with the multiple passes of a low-energy ion beam. The FIB-induced damage was minimized by cleaning at 2 kV and 48 pA.

Atom probe tomography (APT) measurements were performed using a CAMECA LEAP 5000XR instrument in laser pulsing mode at 60 K tip temperature, employing 30 pJ laser pulse energy at a repetition rate of 250 kHz. Post measurement, the data were analyzed using IVAS 3.6.10a software provided by Cameca Instruments. Samples for APT were prepared using an FEI Scios focused-ion beam (FIB) SEM.

Nanoindentation experiments were conducted using Hysitron Triboindenter (Hysitron, Inc., Minneapolis, MN) with a Berkovich diamond tip at room temperature. To compensate for potential tip blunting from prior use, the tip radius was calibrated by fitting the elastic loading section of the indentation data (over a 4×4 indentation grid) to the Hertzian contact theory[43] using a standard fused quartz sample. The effective radius was determined to be 260.82 ± 9.41 nm. To study the first pop-in behavior of the present MPEA, indentation tests were carried out at three different loading rates (25, 250, and 2500 μN/s). To assess the impact of crystal orientation, grains close to (001), (110), and (111) were identified using EBSD and subsequently indented. To eliminate the influence of the grain boundary, all tests were conducted in the grain far away from the grain boundary. A loading function was utilized under an open-loop condition, with a constant loading rate segment up to a peak load of 10000 μN, followed by a peak load holding segment for 10 seconds and a constant unloading rate segment. Around 40 to 50 indents were performed in each grain with 10 μm intervals to avoid any overlap of plastic zones created by neighboring indentations.

III. RESULTS AND DISCUSSION

A. *Undeformed Microstructure Characterization*

Figure 1(a) displays the XRD pattern acquired using a section of the cast and homogenized $Co_{21.5}Cr_{21.5}Fe_{21.5}Mn_{21.5}Ni_{14}$ MPEA. The XRD pattern reveals sharp diffraction peaks corresponding to a deformation-free single-phase FCC solid solution. The (111) indexed peak demonstrates relatively high intensity, suggesting the existence of a minor texture. The lattice parameter (a) was determined to be ~ 3.586 Å, which is slightly lower than that of equiatomic CoCrFeMnNi (~ 3.61 Å [30]).

Figure 1(b) shows the EBSD inverse pole figure (IPF) map acquired after homogenization treatment. The IPF map exhibits near equiaxed grains with a grain size of 500 to 600 μm, which is adequate for conducting the indentation experiments. In addition, the texture observed in the XRD pattern is also evident from the EBSD analyses. Evidently, the IPF map exhibits a slight $< 111 >$ texture.

To observe $Co_{21.5}Cr_{21.5}Fe_{21.5}Mn_{21.5}Ni_{14}$ microstructure at a higher resolution, TEM investigations were conducted. Figure 1(c) shows a bright-field TEM micrograph acquired from FIB-prepared TEM lamella close to the electropolished specimen surface. The corresponding diffraction pattern is shown in the inset. As evident, no secondary phase, clusters, and dislocations could be observed. To further examine the distribution of constituent elements at the nanoscale, APT investigations were performed. The three-dimensional reconstructions obtained from the analyzed volume in Figure 1(d) confirm the homogenous distribution of elemental constituents without any clustering or segregation. Overall, it can be stated that the mechanical response described later is representative of a homogenized FCC solid solution.

B. *Nanoindentation and Incipient Plasticity*

Figure 2(a) shows a representative load–displacement (P–h) curve obtained under 250 μN/s loading rate from a grain-oriented close to (111) orientation. For clarity, only the loading portion at shallow depth is shown. Evidently, the load–displacement curve exhibits two distinct regions: elastic and elastic-to-plastic transition regions. Furthermore, the elastic-to-plastic transition region shows a discontinuity at a constant load, referred to as a pop-in event or incipient plasticity. Prior to the first pop-in event, the deformation is purely elastic (recoverable) and follows a Hertzian contact theory.[43] As per the theory, the equation below characterizes the elastic response of a sample surface to a spherical contact.

$$P = \frac{4}{3} E_r R^{\frac{1}{2}} h^{\frac{3}{2}} \quad [1]$$

where P is the applied load, R is the indenter tip radius, h is the contact depth measured from the sample surface to the bottom of the indenter sample contact, and E_r is the reduced modulus of the sample-indenter combination. E_r is derived as

$$\frac{1}{E_r} = \frac{1 - \nu^2}{E} + \frac{1 - \nu_i^2}{E_i} \quad [2]$$

Here, E and ν are the elastic modulus and Poisson's ratio of the sample, whereas $E_i = 1141$ GPa, $\nu_i = 0.07$ are the elastic modulus and Poisson's ratio of indenter.

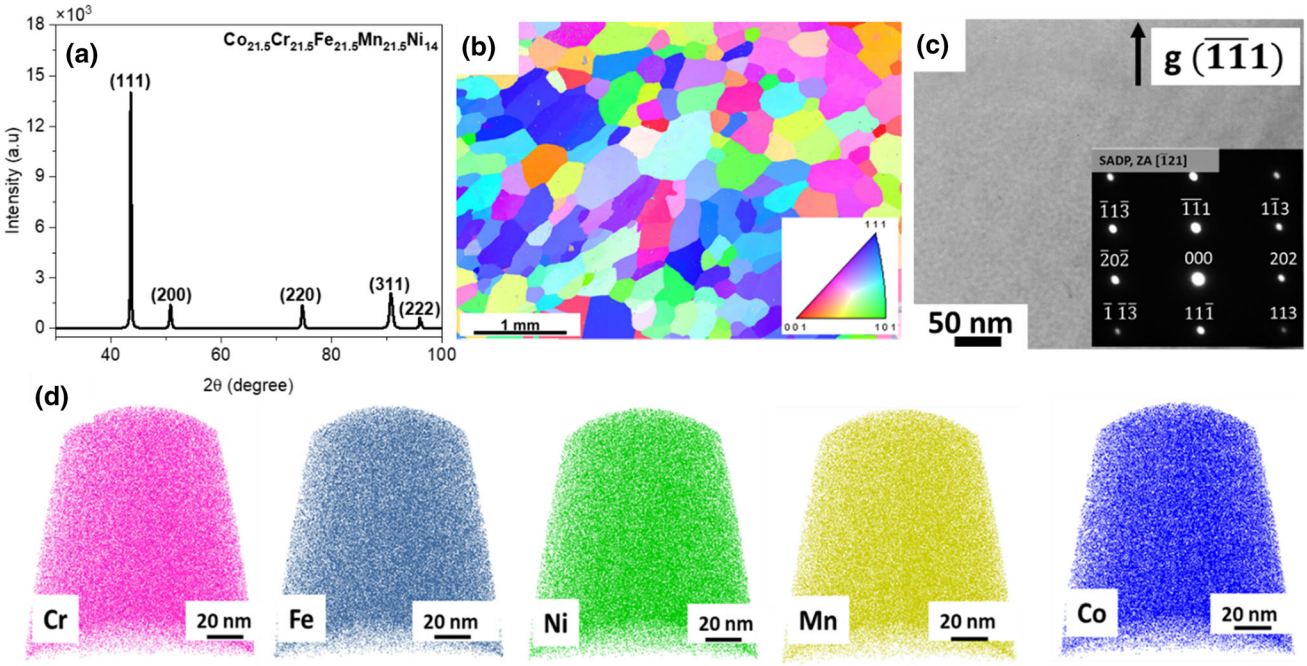

Fig. 1—(*a*) XRD pattern exhibits sharp diffraction peaks corresponding to an FCC solid solution with slight < 111 > texture. (*b*) EBSD-IPF map also shows minor < 111 > texture with near equiaxed grains. The color key is presented as an inset in the lower right corner of the IPF map. (*c*) Bright-field TEM micrograph acquired near the sample surface along the [$\bar{1}$21] zone axis reveals a defect-free microstructure without any secondary phase. The selected area diffraction pattern acquired close to the [$\bar{1}$21] zone axis is shown as an inset at the bottom right corner. (*d*) APT three-dimensional reconstructions reveal homogenous distribution of elemental constituents without clustering or segregation.

The Hertzian fitting of the elastic region with Eq. [1] is also shown in Figure 2(a). The fitting resulted in a fitting coefficient of 4.27 with a standard deviation of 0.25. The corresponding reduced modulus from Eq. [1] was calculated to be 198.29 GPa.

A different approach to calculate the reduced modulus involves using statistical fitting. For this, a set of *P*-*h* pairs from 40 to 50 indentations in the same grain at the pop-in stage are gathered and plotted in a P–$h^{3/2}$ graph based on Eq. [1], as illustrated in Figure 2(b). Evidently, the first pop-in load ranges from 67.12 to 120.16 μN and the pop-in depth ranges from 6.02 to 9.23 nm. This suggests that pop-ins are a statistical process that exhibits stochastic behavior and is affected by various microstructural factors at the local level.[44,45] These factors include interstitial atoms, vacancies, pre-existing dislocations, sub-grain boundaries, and surface roughness at the sub-atomic level.

The linear fitting of *P*–*h* pairs resulted in a fitting coefficient of 4.22 with a standard deviation of 0.04 and the reduced modulus as 197.97 ± 4.15 GPa. Both methods are consistent and result in a statistically similar value of reduced modulus. Compared to the equiatomic CoCrFeMnNi,[30] the obtained reduced modulus is higher, which could be associated with the investigated MPEA's lower lattice parameter.

To further analyze incipient plasticity, the maximum shear stress (τ_{max}) beneath the indenter was measured according to the Hertzian contact problem.[26,46,47] τ_{max} is calculated from the mean pressure (p_m) under the indenter at pop-in as:

$$p_m = \left(\frac{6PE_r^2}{\pi^3 R^2}\right)^{\frac{1}{3}} \quad [3]$$

$$\tau_{max} = 0.31 p_m \quad [4]$$

where P is the load at pop-in. A statistical plot in Figure 2(c) depicts the cumulative probability distribution of the pop-in events as a function of maximum shear stress. As maximum shear stress (or pop-in loads) increases, the gradual increase in cumulative probability is evident. This can be attributed to the significant role played by the above-mentioned local factors, especially at lower pop-in loads. The calculated τ_{max} ranges from 5.89 to 7.42 GPa with an average value of 6.64 ± 0.43 GPa, which lie in between $\frac{\mu}{13}$ to $\frac{\mu}{10}$, where μ is the shear modulus. Note that due to the unavailability of data for the current alloy composition, the shear modulus (μ = 77 GPa[31]) of the CoCrFeMnNi and Poisson's ratio of 0.3 (by assuming as an isotropic solid) has been considered throughout this work for the sake of convenience. The obtained maximum shear stress falls within the order of the material's theoretical shear strength ($\frac{\mu}{30}$ to $\frac{\mu}{5}$),[48–52] indicating the onset of yield may be caused by the dislocation nucleation mechanism. In addition, the studied MPEA shows slightly higher τ_{max} than equiatomic CoCrFeMnNi,[30] which may be ascribed to its higher shear modulus, a larger misfit volume due to the presence of higher percentage of Cr,[53,54] and a higher extent of solid solution hardening.[11] This finding provides further evidence that the

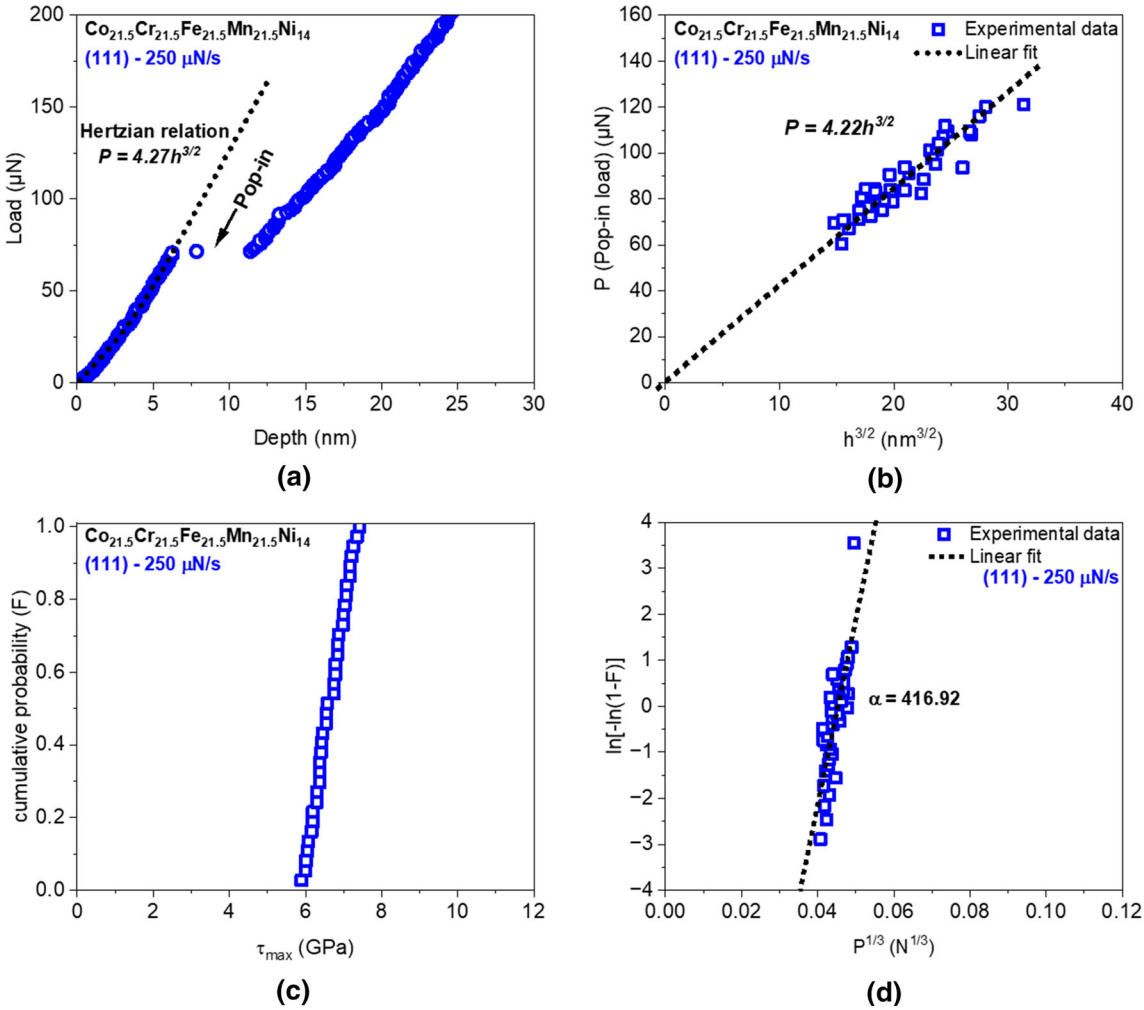

Fig. 2—(*a*) A representative load–displacement (*P-h*) curve obtained under 250 μN/s loading rate from a grain-oriented close to (111) orientation. The elastic portion of the curve is fitted with Hertzian contact equation Eq. [1]. (*b*) Statistical plot of $P\text{-}h^{3/2}$ pairs at pop-in. The fitting yields a fitting coefficient of 4.22. (*c*) Cumulative probability of pop-in events as a function of maximum shear stress. (*d*) A first-order analytical solution to generate α which is substituted in Eq. [6] to calculate the activation volume (V).

incipient plasticity of MPEAs is affected by their specific chemical bonding characteristics.

The cumulative distribution function, F, can be further utilized to compute the activation volume for the rate-determining event that controls plasticity. Schuh *et al.*[26,27] proposed a connection between the cumulative probability function $F(P)$ and the first pop-in load through a first-order analytical solution as:

$$\ln[-\ln(1-\mathrm{F(P)})] = \alpha \mathrm{P}^{\frac{1}{3}} + \beta \qquad [5]$$

where α is the slope of the $\ln[-\ln(1-\mathrm{F(P)})]$ *vs* $P^{\frac{1}{3}}$ plot shown in Figure 2(d) and β is a weak function of pop-in load.[26,30,38] The α is linked to the activation volume (V) through Eq. [6].

$$V = \frac{\pi}{0.47}\left(\frac{3R}{4E_r}\right)^{\frac{2}{3}} kT \cdot \alpha \qquad [6]$$

where k is Boltzmann's constant, and T is the test temperature. The slope value of the plot presented in Figure 2(d) is determined to be 416.92, and V is evaluated to be 11.44 Å^3, which in terms of atomic volume (Ω) comes out to be $V = 1.07\ \Omega$, based on the present MPEA's lattice parameter of 3.586 Å.

C. *Effect of Loading Rate*

To investigate how loading rate affects pop-in behavior in the current MPEA, a grain that exhibits an orientation close to (111) was chosen for indentation testing. The tests were conducted under three different loading rates, namely 25, 250, and 2500 μN/s. A statistical linear fitting of P–$h^{3/2}$ pairs at pop-in is shown in Figure 3. Evidently, a clear dependency of pop-in load and displacement on loading rate is observed. Although the pop-in load and displacement varied around a similar range, the minimum and maximum loads shifted toward higher values with an increase in the loading rate. Hence, it can be concluded that the average first pop-in load and the displacement increase with an increased loading rate (see Table I).

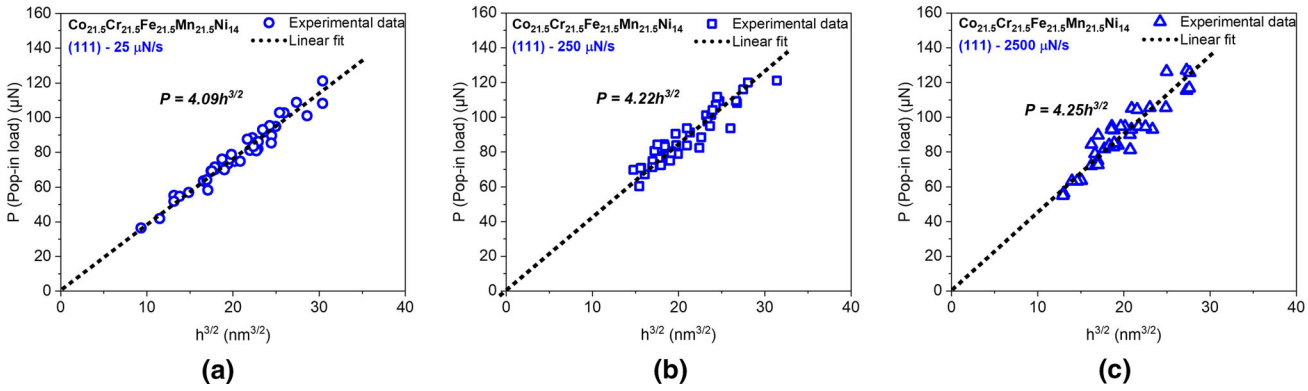

Fig. 3—Statistical linear fitting of P–$h^{3/2}$ pairs at pop-ins for loading rates (*a*) 25 μN/s, (*b*) 250 μN/s, and (*c*) 2500 μN/s. The fitting yields a fitting coefficient of 4.09, 4.22, and 4.25 for loading rates of 25 μN/s, 250 μN/s, and 2500 μN/s, respectively.

The possible reason for such a loading rate dependency can be ascribed to the fact that pop-in is not only a stress-assisted but also a thermally activated process.[27] In other words, the energy barrier for dislocation nucleation might be overcome by both the mechanical work of indentation and an appropriate thermal fluctuation. The observed scatter in the pop-in event is likely the result of thermal fluctuations that occasionally favor dislocation nucleation and sometimes do not. As a result, the probability of the pop-in event within a specific load range can be discussed. Additionally, with the increase of the loading rate, the pop-in load increases. This is due to the fact that the probability of overcoming the energy barrier by thermal fluctuations decreases; since the time to reach the pop-in load decreases. Contrary to the pop-in load's dependence on the loading rate, no appreciable variation in the elastic modulus with the loading rate was observed. Similar results have also been reported in both simulations[55] and experimental studies conducted on pure metals,[26,27] BCC MPEA[36–38,56] and FCC CoCrFeMnNi MPEA.[30]

The cumulative probability distribution of the pop-in events at three investigated loading rates are plotted as a function of maximum shear stress in Figure 4(a). As evident, the maximum shear stress at first pop-in events shifts toward the higher load with increasing loading rates. Additionally, there is significant overlap in the 250 and 2500 μN/s curves at lower loads ($F < 0.5$), which suggests that these indents are more likely influenced by comparable local factors. The α values determined from the $\ln[-\ln(1-\mathrm{F(P)})]$ *vs* $P^{\frac{1}{3}}$ plots as presented in Figure 4(b) through (d) for three loading rates are used for calculating the activation volume according to Eq. [6]. It was found that the activation volume varies slightly with the loading rate but lies within the same order of magnitude ranging from 10.35 to 11.44 Å^3, *i.e.*, 0.9 to 1.07 Ω (see Table I). This indicates that the dominant mechanism driving incipient plasticity in the present MPEA remained unchanged, regardless of the loading rate. Similar results were also observed for BCC MPEA.[56]

D. *Effect of Grain Orientation*

To study the effect of orientation on pop-in behavior in the current MPEA, three grains close to (001), (110), and (111) orientations were identified. Several indents were performed on each grain under a loading rate of 2500 μN/s (see Figure 5). The typical load–displacement (P–h) curves at shallow depths from three different grains are presented in Figure 5(d). Each curve is displaced along the x-axis. Only the loading portions are shown for clarity. The P–h curves represent the general trend observed for three orientations. Evidently, there is a clear dependency of pop-in load and displacement on orientation, which vary from indentation to indentation, showing stochastic yield behavior. The load and associated displacement for all three orientations show a near-normal distribution, which is presented in Figure 6. The distribution of pop-in load and associated displacements for all three orientations varies between 39.95 and 127.17 μN and 4.41 to 9.14 nm, respectively. However, from Table II, the average pop-in load and associated average displacement are highest for (111) orientation, followed by (110) and (001) orientations, respectively. This indicates that the stochastic nature of incipient plasticity in the current MPEA is influenced by grain orientation, and (111) requires ~ 32.1 pct and ~ 18.7 pct higher pop-in load and displacement than (001) to initiate the plasticity. The reasons for these observations will be discussed in the following subsection.

Additionally, it is essential to consider the effect of grain orientation on the indentation modulus or reduced modulus (E_r) as the deformed volume is very small; the crystal anisotropy effect will become more pronounced. The statistical linear fitting of P–$h^{3/2}$ pairs at pop-ins in three different orientations is shown in Figure 7. The slope of the fitted dotted line yields a fitting constant of 3.82, 3.97, and 4.25 for P–$h^{3/2}$ pairs of grains close to

Table I. A Summary of First Pop-in Load, Displacement, Reduced Modulus, Maximum Shear Stress, and Activation Volume Obtained for Grain-Oriented Close to (111) Orientation Under a Loading Rate of 25 μN/s, 250 μN/s, and 2500 μN/s

Loading rate	25 μN/s	250 μN/s	2500 μN/s
Pop-in load, P (μN)	78.67 ± 17.86	82.88 ± 21.39	89.63 ± 18.66
Pop-in displacement, h (nm)	7.47 ± 1.17	7.15 ± 1.40	7.30 ± 1.00
Pop-in length (nm)	5.48 ± 2.05	5.83 ± 2.43	5.95 ± 1.77
Reduced modulus (E_r) (GPa)	189.93	195.97	197.36
Maximum shear stress (τ_{max}) (GPa)	5.90 ± 0.50	6.63 ± 0.43	7.02 ± 0.68
Activation volume (V) ($Å^3$)	10.35 = 0.90 Ω	11.44 = 1.07 Ω	11.32 = 0.98 Ω

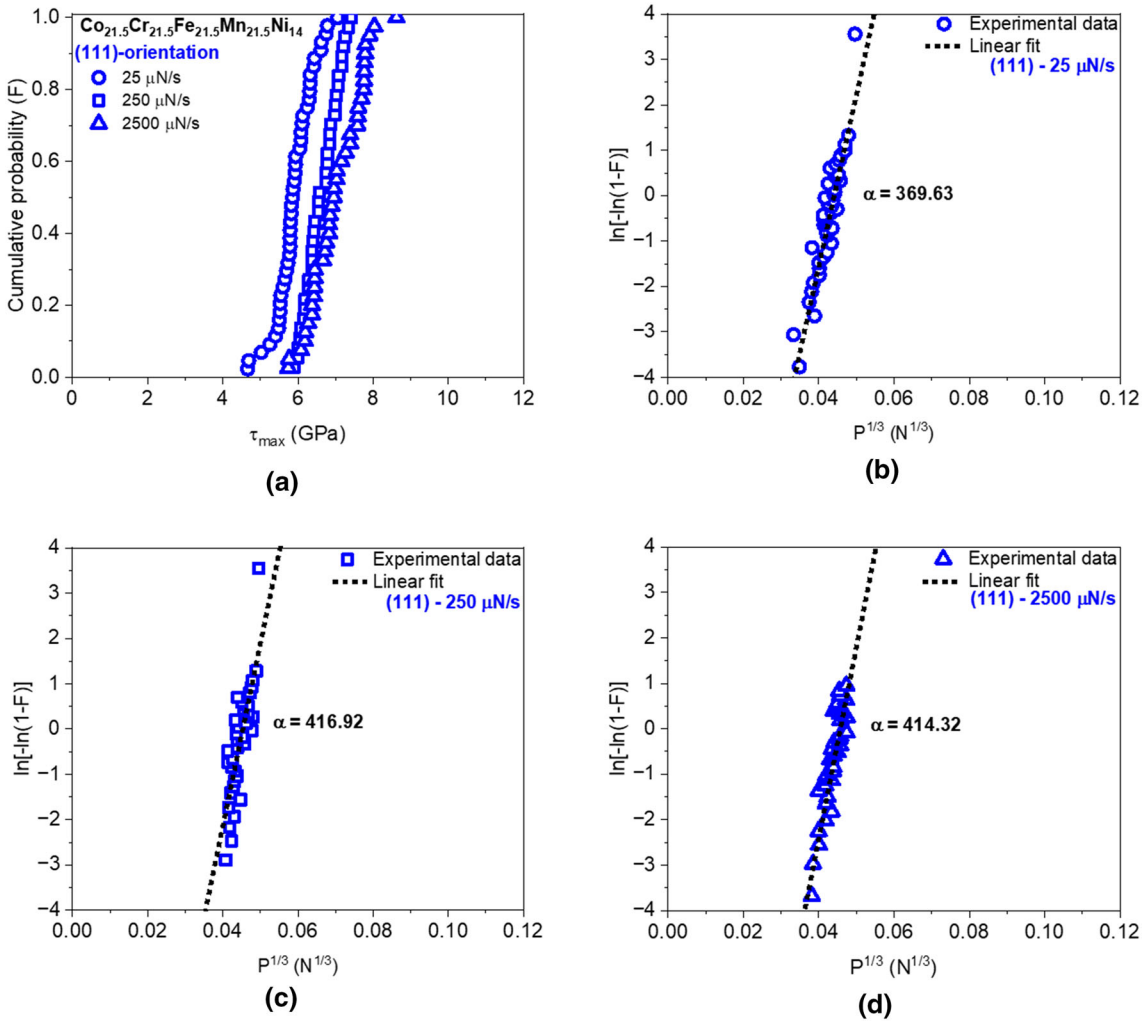

Fig. 4—(*a*) The cumulative probability of pop-in events as a function of maximum shear stress for 25 μN/s, 250 μN/s, and 2500 μN/s loading rates. (*b*) through (*d*) The slope of the $\ln[-\ln(1-F(P))]$ *vs* $P^{\frac{1}{3}}$ plots used for extracting the α values for three different loading rates (b) 25 μN/s (c) 250 μN/s (d) 2500 μN/s.

(001), (110) and (111) orientations, respectively. According to Eq. [1], the calculated E_r of three orientations have been listed in Table II. It is evident that the orientation of the grain has a noticeable effect on the E_r, *i.e.*, it exhibits elastic anisotropy with (001) and (111) showing the lowest (~ 170.12 GPa) and highest (~ 197.36 GPa) modulus, respectively.

The cumulative probability distributions of the pop-in events in grains oriented close to (001), (110), and (111) orientations are plotted as a function of maximum shear stress (τ_{max}) in Figure 8(a). The average maximum shear stress for the three studied orientations is listed in Table II. Evidently, the (111) oriented grain has the highest τ_{max}, followed by almost similar for (110) and

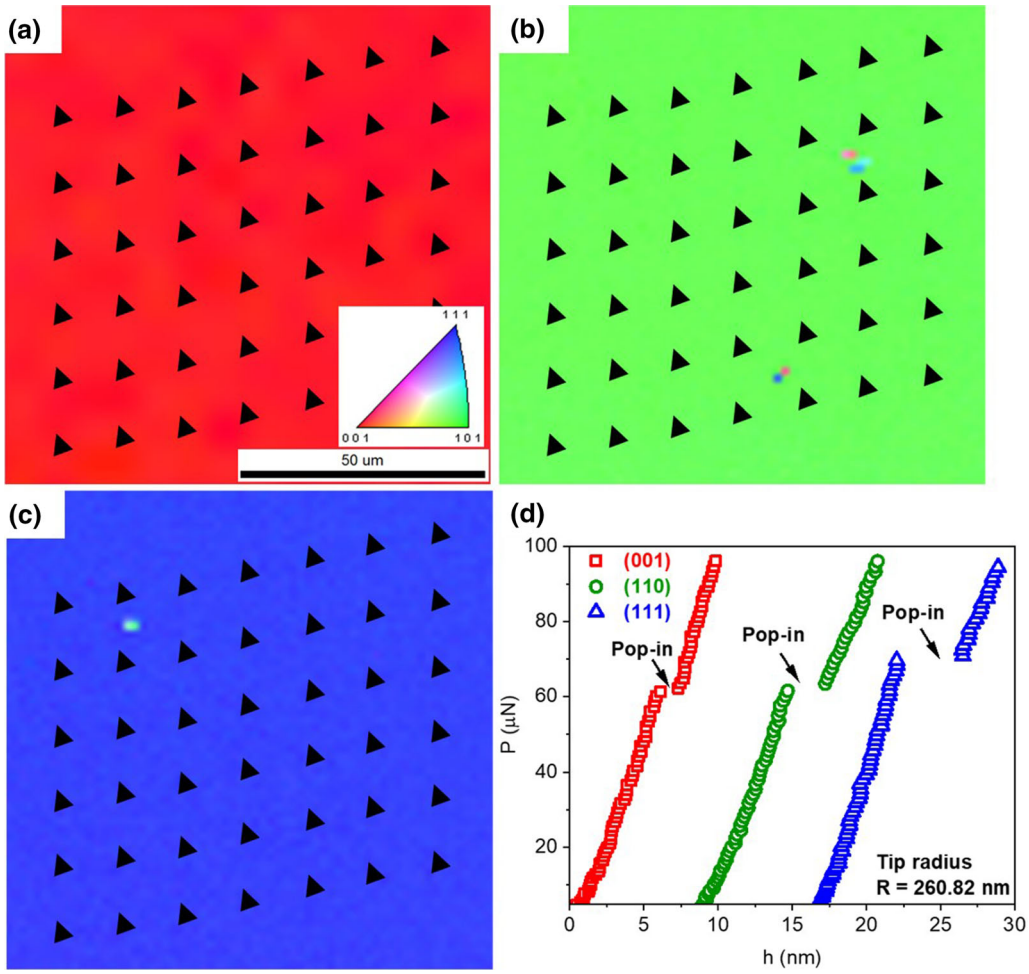

Fig. 5—EBSD-IPF maps with overlayed schematic indents from three grains close to (*a*) (001), (*b*) (110), and (*c*) (111) orientations. (*d*) The typical load–displacement (*P*–*h*) curves from three differently oriented grains. Curves are off set from the origin for clarity. A dependence of pop-in load and associated displacement on grain's orientation is apparent.

(001), implying that the onset of plasticity is orientation dependent. Overall, the τ_{max} lies in the range of $\frac{1}{13}$ to $\frac{1}{10}$ of the shear modulus. Following similar steps, as mentioned before, the α values determined from the $\ln[-\ln(1-F(P))]$ *vs* $P^{\frac{1}{3}}$ plots, as presented in Figures 8(b) through (d) for three orientations, are used for calculating the activation volume according to Eq. [6]. Like the loading rate effect, the activation volume varies slightly with the orientation but lies within the same order of magnitude (Table II), ranging from 10.72 to 11.32 $\mathring{A}^3$, *i.e.*, 0.92 to 0.98 Ω (around one atomic volume). This indicates that the dominant mechanism driving incipient plasticity in the present MPEA remained unchanged, regardless of the grain orientation.

E. *Incipient Plasticity Mechanism, Orientation Effect, and Comparison with Pure Metals and Other MPEAs*

The onset of plasticity in crystalline materials, which manifests as the pop-in during nanoindentation, may occur either by the slip of pre-existing mobile dislocations or by dislocation nucleation. The pre-existing dislocations may be present due to the inability to completely remove them during homogenization or the possibility of new ones arising during sample polishing. However, considering that well-annealed metals and alloys usually exhibit a dislocation density of approximately 10^{10} to 10^{12} m^{-2},[57] it follows that the distance between dislocations is about 1 to 10 μm, which is considerably larger than the typical size of the stressed zone beneath the indenter (estimated as $\sim \pi a_c^3 = \sim 0.00026\ \mu m^3$, where $a_c = \sim \sqrt{Rh_c} = \sim 44.13$ nm where R is the tip radius and h_c is the average pop-in depth). Hence, the probability of finding a pre-existing dislocation in the highly stressed volume is low. Although even if indentation could have occurred in or near areas of pre-existing dislocations, the critical resolved shear stress for dislocation slip in FCC MPEAs, such as equiatomic CoCrFeMnNi (*e.g.*, ~ 33 to 43 MPa[10]), is much lower than the measured shear stress (lying in between ~ $\frac{\mu}{13}$ and $\frac{\mu}{10}$, which falls within the range of the theoretical shear strength of the material[51,52]). Therefore, it is less likely that the pop-in

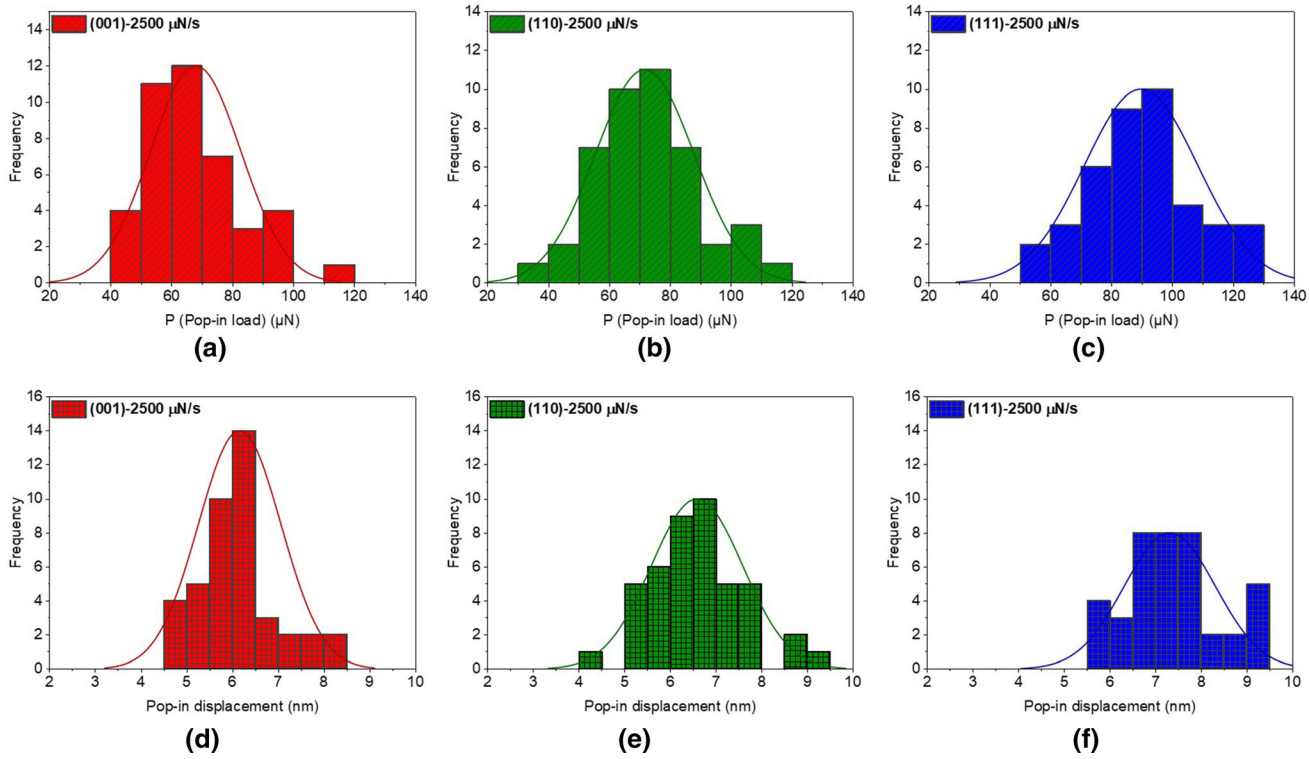

Fig. 6—(*a*) through (*c*) Distribution of pop-in loads and (*d*) through (*f*) Distribution of pop-in displacements measured for grains oriented close to (001), (110), and (111) orientations.

Table II. A Summary of First Pop-in Load, Displacement, Reduced Modulus, Maximum Shear Stress, and Activation Volume Obtained Under 2500 μN/s Loading Rate for the Grains Oriented Close to (001), (110), and (111) Orientations

Orientation	(001)	(110)	(111)
Pop-in load, P (μN)	67.85 ± 14.87	71.57 ± 16.20	89.63 ± 18.66
Pop-in displacement, h (nm)	6.15 ± 0.90	6.58 ± 1.0	7.30 ± 1.0
Pop-in length, h (nm)	4.10 ± 1.78	4.30 ± 1.67	5.75 ± 1.77
Reduced modulus (E_r) (GPa)	170.12 ± 10.65	176.77 ± 15.14	197.36 ± 3.95
Maximum shear stress (τ_{max}) (GPa)	6.23 ± 0.54	6.28 ± 0.59	7.02 ± 0.68
Activation volume (V) (A^3)	10.72 = 0.92 Ω	11.10 = 0.96 Ω	11.32 = 0.98 Ω

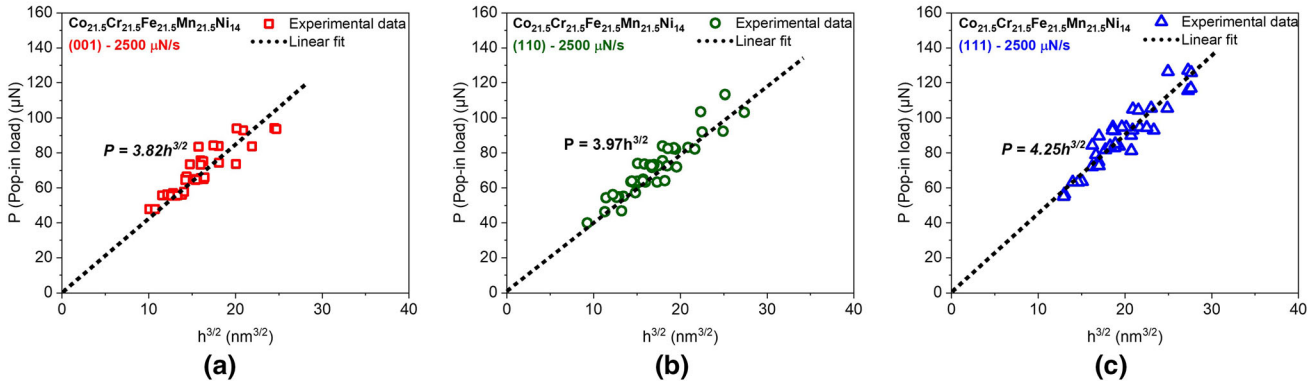

Fig. 7—Statistical linear fitting of P–$h^{3/2}$ pairs for pop-ins measured from grains close to (*a*) (001), (*b*) (110), and (*c*) (111) orientations under a loading rate of 2500 μN/s. The fitting yields a fitting coefficient of 3.82, 3.97, and 4.25 for (001), (110), and (111) orientations, respectively.

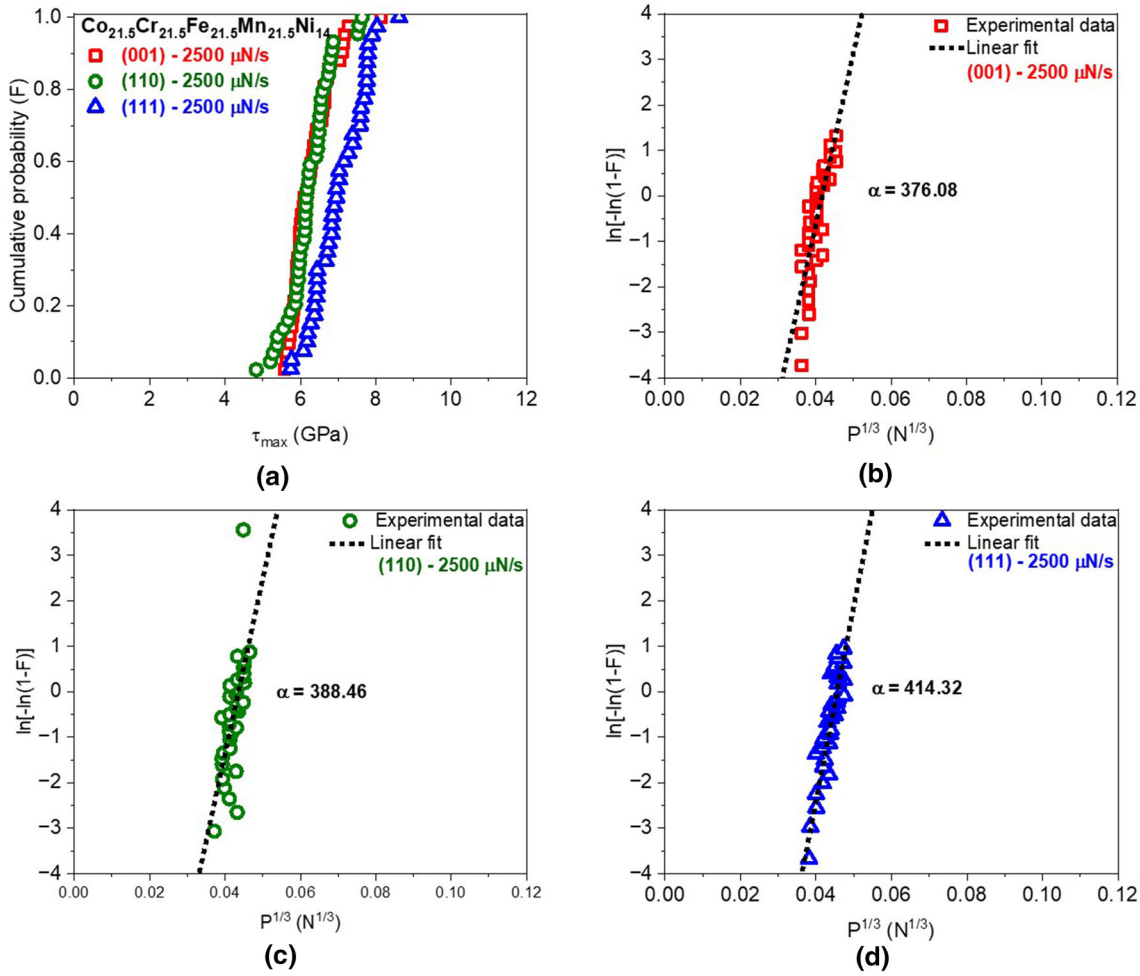

Fig. 8—(*a*) The cumulative probability of pop-in events as a function of maximum shear stress for (111), (110), and (001) orientated grains under 2500 μN/s loading rate. (*b*) through (*d*) The slope of the $\ln[-\ln(1-F(P))]$ *vs* $P^{\frac{1}{3}}$ plots used for extracting the α values from experimental data obtained grains oriented close to (001), (110), and (111) orientations under 2500 μN/s loading rate.

occurred due to the movement of pre-existing mobile dislocations and more likely it is caused by the nucleation of dislocations.

Indeed, TEM investigations conducted beneath the nanoindent impression showed a high density of dislocations in the deformed volume, see Figures 9(a) and (b), which was not observed prior to indentation, see Figure 1(c). The primary deformation mode was identified to be the planar slip of dislocation arrays along {111} planes, as shown in Figure 9(b). Similar observations have also been reported before for low SFE equiatomic CoCrNi MPEA[33] and Fe−20Cr–25Ni austenitic alloy,[58] which is known to cause glide plane softening.[33] Additionally, several stacking faults (SFs) oriented close to a 45 deg angle to the loading axis, corresponding to the direction of maximum shear stress, were observed (see Figure 9(c)). The presence of planar slip and SFs can be attributed to the low SFE of the $Co_{21.5}Cr_{21.5}Fe_{21.5}Mn_{21.5}Ni_{14}$ MPEA. The formation of SFs upon indenting (111) surface is consistent with the results of molecular dynamics (MD) simulations conducted on pure metals having low SFE, including Au,[59] and Cu, which suggests presence of partial dislocations.[60] In summary, it can be inferred that the observed displacement bursts are an intrinsic behavior of the studied MPEA and are related to the phenomenon of dislocation nucleation. The possibility of incipient plasticity resulting from phase transformation,[21] matrix cracking,[22] or oxide film cracking[23–25] can be eliminated, as no such phenomena were observed.

Dislocation nucleation can either occur *via* homogeneous or heterogeneous mechanisms. For homogenous dislocation nucleation, the initial pop-in event is suggested to involve the cooperative movement of a few atoms to form a critical-sized dislocation loop.[27,61] The activation volume for such a mechanism is generally suggested to be less than one atomic volume, as the critical size of the dislocation loop may diminish substantially when the applied stress approaches measured shear stress, lying in between ~ $\frac{1}{13}$ and $\frac{1}{10}$ of the shear modulus, which is around the theoretical shear strength of the alloy.[26,61] Moreover, as mentioned earlier, a scenario of homogeneous dislocation nucleation is possible in annealed materials, where the likelihood of finding a pre-existing dislocation in the

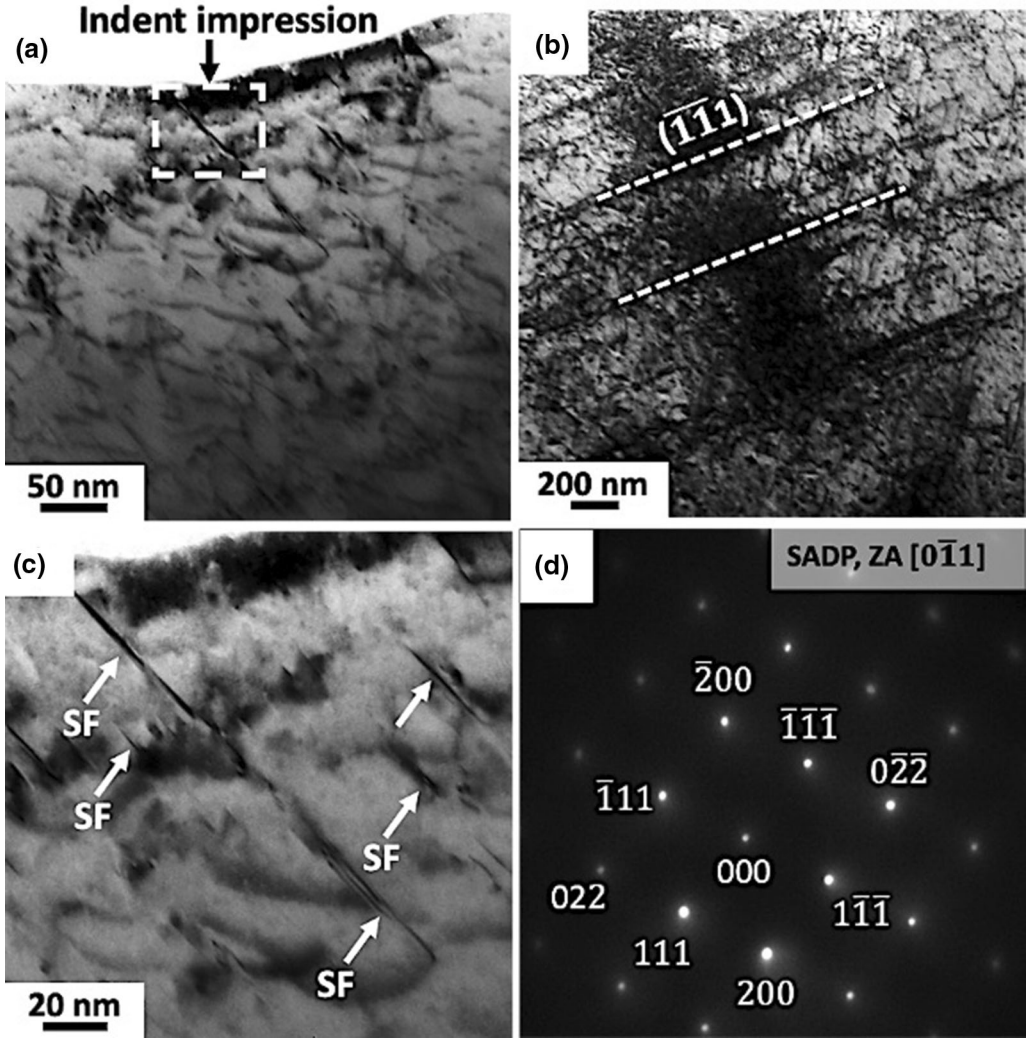

Fig. 9—(*a*) BF-TEM micrograph presents a cross-sectional view of the lift-out sample taken close to the center of a nanoindent, performed under 250 μN/s loading rate from a grain-oriented close to (111) orientation. (*b*) BF-TEM micrograph, acquired under two-beam condition with g close to ($\bar{1}\bar{1}1$), beneath the nanoindent impression from a location just below the one depicted in (a), presents dislocation arrays resulting from planar slip along {111} planes in the deformed volume. (*c*) A magnified view of the marked plastic zone adjacent to the indent impression in (a) shows several stacking faults (SFs), which are aligned 45 deg to the loading axis. (*d*) Selected area diffraction pattern (SADP) captured near the [0$\bar{1}$1] zone axis from the deformed volume shows no additional diffraction spots other than those corresponding to the single-phase FCC matrix, thereby confirming the absence of any phase transformation during indentation. Note that all BF micrographs are acquired close to [0$\bar{1}$1] zone axis.

highly stressed volume is low. Nevertheless, the activation volume in the current study is determined to be around one atomic volume (~ 1 Ω = ~ 0.70 b^3), which is comparable to the size of a vacancy (~ 0.67 b^3),[62] when considering full dislocations. This suggests that apart from homogenous, heterogenous nucleation mechanisms might also be active. Indeed, activation volume greater than or equal to 1Ω is usually attributed to the heterogeneous dislocation nucleation aided by pre-existing dislocations, vacancies (or vacancy clusters), impurities, and/or surface asperities/ledges.[63,64] In addition, the displacement excursion during the first pop-in event is several nanometers, which is too large to be accounted for by the movement of just a few atoms.

To gain a better understanding of the mechanisms, the distribution of the shear stress at yield (or pop-in), τ_{max}, from the nanoindentation data can be analyzed. One approach to describe this distribution is through kernel density estimation (KDE),[65] which would typically yield a symmetric, Gaussian-type unimodal distribution for thermally activated, stress-assisted pop-in behavior.[31,66] Figure 10 displays the Gaussian KDE distributions of the maximum shear stress (τ_{max}) data obtained from indentation tests performed on a grain with an orientation near (111) at loading rates of 25 μN/s, 250 μN/s, and 2500 μN/s. Interestingly, the KDE distributions in the current study overlap substantially and exhibit "shoulder" peaks, indicating bimodal characteristics. Bimodal distributions of τ_{max} have also been reported in previous studies on equiatomic CoCrNi, CoCrFeNi, and CoCrFeMnNi MPEAs, which are associated with the activation of more than one deformation mechanism.[31,33] Moreover, the shoulder peak at the lower values of τ_{max} are ascribed to the

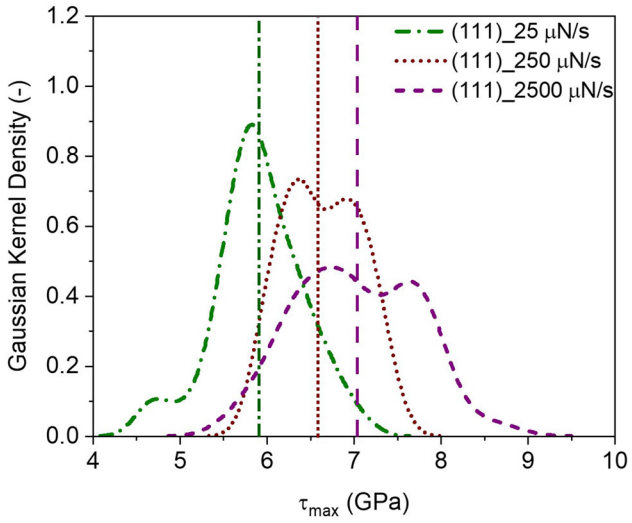

Fig. 10—Kernel density curves at first pop-ins for tests performed on a grain with an orientation near (111) at loading rates of 25 μN/s, 250 μN/s, and 2500 μN/s. Evidently, bimodal KDE distribution shifts toward higher τ_{max} values and become wider with increasing loading rate. The dashed line marks the average τ_{max} value at each loading rate which increases with loading rate.

heterogeneous nucleation of dislocations through pre-existing defects.[31,33] Meanwhile, the shoulder peak at higher values of τ_{max} are ascribed to homogenous dislocation nucleation. Additionally, Figure 10 reveals that as the loading rate increases, the KDE distribution shifts toward higher τ_{max} values and becomes wider. The average τ_{max} value also shows an increase with loading rate, which aligns with the findings presented in Section C. The changes in the height of the peaks at varying loading rates indicate that the fraction of nucleation mechanisms is dependent on the loading rate. This warrants further investigations to better understand this relationship. Overall, it is suggested that in the current alloy, a combination of the mechanisms mentioned above is responsible for the pop-in event, including the heterogeneous nucleation of dislocations through pre-existing precursors.

Further, the burst of crystal displacement is significantly influenced by the crystalline orientation, with the pop-in load and displacement being orientation-dependent. It is well established that crystal anisotropy becomes more pronounced as the deformed volume decreases.[67–69] For FCC metals, such as Ag, Al, and Cu, previous simulation studies have demonstrated that the (111) orientation yields the highest pop-in loads, while the (001) orientation results in the lowest loads.[60,70] Similar results are also obtained for the present MPEA, with the (111) orientation showing the highest pop-in loads, displacements, and maximum shear stresses, followed by the (110) orientation, and finally, the (001) orientation, which showed the lowest values (see Table II). Moreover, the effective reduced modulus followed the same trend, with the (111) orientation having the highest value, followed by the (110) orientation, and finally, the (001) orientation. Multiple factors can explain this orientation effect.

(i) When the critical indentation depth is reached, a significant amount of elastic energy accumulates due to the higher stiffness of the (111) orientation. This, in turn, triggers a more intense dislocation avalanche, resulting in a larger displacement jump during plastic deformation. Furthermore, MD simulation[60] revealed early nucleation of a single SF under (001) orientation, which continued to grow during further indentation. For the other two orientations, the nucleation of dislocations occurs later.[60]

(ii) Multiple slip systems must be initiated to meet the plastic deformation of the indentation geometry, and when the indenter probes the crystal on different orientations, the number of activated slip systems and resolved shear stresses on each slip system would be different, leading to a different density and configuration of dislocations.[59,60,71]

Additionally, the relative orientation of the crystal surfaces to the primary slip systems plays a crucial role in plasticity. The Schmid factor is a key parameter that determines the active slip systems, with those with the largest one becoming active first. Tables III and IV present the largest Schmid factors for each plane and the possible slip system for full and partial dislocations, respectively. The largest Schmid factors for (001) and (110) are higher in value for both full and partial dislocations, whereas for (111), it is lower. Considering the case of partial dislocations, the experimental results deviate from the expectations based on Schmid factors. Although the (110) orientation exhibits the highest Schmid factor among the potential slip systems for partial dislocations (see Table IV), the observed pop-in load, displacement, and shear stress for this orientation fall between those of the (001) and (111) orientations (see Table II). This indicates a more complex indentation behavior, suggesting the influence of additional factors such as the position of maximum shear stress beneath the indenter,[59,60] the presence of multiple primary nucleation sites,[60] and non-Schmid factors[72,73] in describing the process of dislocation nucleation. However, it still holds true for both full and partial dislocations that applying an indentation downward load or stress on the (111) orientation will generate higher shear stress on all feasible slip systems. To induce the first dislocation activity and initiate plasticity, a higher applied load or shear stress is required for (111) than for (001) and (110), as observed in Table II. The τ_{max} value for (111) is about 7.02 GPa, which is larger than that for (001) and (110) at about 6.28 and 6.23 GPa, respectively. Although the applied downward load or stress on the nanoindentation Berkovich diamond tip is not the same as normal stress used in micropillars, the initial indentation load and stress can still be analyzed based on the magnitude of the resolved shear stress on each slip system. Therefore, the different Schmid factors for each loading plane are the leading cause of the crystalline orientation effects.

Table V shows the activation volume of dislocation nucleation determined by nanoindentation for several

Table III. Largest Schmid Factors for the Possible Activated Slip Systems for the Three Planes, Considering Full Dislocation

Plane	Full Dislocation Slip System	Largest Schmid Factor
(001)	{111} <110>	0.41
(110)	{111} <110>	0.40
(111)	{111} <110>	0.27

Table IV. Largest Schmid Factors for the Possible Activated Slip Systems for the Three Planes, Considering Partial Dislocation

Plane	Partial Dislocation Slip System	Largest Schmid Factor
(001)	{111} <112>	0.47
(110)	{111} <112>	0.66
(111)	{111} <112>	0.30

pure metals, including Ni, Cr, and Pt, as well as equiatomic CoCrFeMnNi and non-equiatomic $Co_{21.5}Cr_{21.5}Fe_{21.5}Mn_{21.5}Ni_{14}$ MPEA. The activation volumes of pure metals and equiatomic CoCrFeMnNi were obtained from studies that employed indenter tips with similar tip radii since the activation volume is known to increase with the tip radius.[20,74] The activation volume for pop-in in the listed MPEAs is considerably higher than that of pure metals, which mainly exhibit a homogeneous dislocation nucleation mechanism. This finding confirms earlier studies by Mridha *et al.*[34] and suggests that incipient plasticity in FCC MPEAs requires the cooperative motion of several atoms rather than one-to-one atomic motion in pure metals. Comparing two MPEAs, the low SFE non-equiatomic $Co_{21.5}Cr_{21.5}Fe_{21.5}Mn_{21.5}Ni_{14}$ exhibits a lower activation volume than the equiatomic CoCrFeMnNi. Similarly, Mridha *et al.*[34] showed significantly lower activation volume for low SFE equiatomic CoCrNi MPEA than equiatomic CoCrFeMnNi. This indicates that the activation volume of the CoCrFeMnNi system is affected by the presence of different-sized atomic species, which are known to influence both the SFE and energy landscapes. This is consistent with the modeling efforts of Xiao *et al.*,[32] which suggested that low SFE MPEA require high athermal stress and low activation volume for dislocation nucleation due to their low critical nucleation radius. Although our experiments could examine several factors that can affect pop-in behavior in low SFE non-equiatomic $Co_{21.5}Cr_{21.5}Fe_{21.5}Mn_{21.5}Ni_{14}$ MPEA and its distinction from pure metals and equiatomic CoCrFeMnNi, a more comprehensive understanding of the nucleation event will require the application of atomistic simulations.

Table V. Activation Volume and Dislocation Nucleation Mechanism in Typical Pure Metals and Equiatomic/Non-equiatomic CoCrFeMnNi Alloys, with Comparable Tip Radius

Material	Sample Surface Processing History	Tip Radius (nm)	Activation Volume (Ω)	Mechanism	Refs.
Ni	Annealed + Vibratory polished	Unknown	0.4	Homogeneous	[34]
Cr	Annealed + Electropolished	210	0.4	Homogeneous	[16]
Pt	As received + Electropolished	150	0.5	Homogeneous	[26]
CoCrFeMnNi	Mechanical polishing + Annealed	233	3	Heterogeneous	[30]
$Co_{21.5}Cr_{21.5}Fe_{21.5}Mn_{21.5}Ni_{14}$	Homogenized + Electropolished	260.8	~ 1	Homogeneous + Heterogeneous	Present work

IV. SUMMARY AND CONCLUSIONS

Nanoindentation experiments were performed on a low SFE $Co_{21.5}Cr_{21.5}Fe_{21.5}Mn_{21.5}Ni_{14}$ MPEA with an FCC crystal structure. The following conclusions are drawn.

1. Indentation pop-in, which marks the onset of yielding, is observed for three different orientations and at every loading rate conducted in this study.
2. Both loading rate and grain orientation influence the initial pop-in event during nanoindentation. Higher loading rates result in higher pop-in loads and displacements, while the (111) orientation demonstrates the highest pop-in load and displacement, followed by (110) and (001) orientations, respectively. Additionally, the (111) orientation has the highest reduced modulus value, followed by (110) and (001) orientations.
3. The maximum shear stress required to cause incipient plasticity was found to be within $\frac{1}{13}$ to $\frac{1}{10}$ of the shear modulus. This range falls within the theoretical shear strength of the material, indicating that the nucleation of dislocations triggered pop-in events. The observation of a high density of dislocations under planar slip and stacking faults beneath the indent through TEM investigations further supports this conclusion.
4. In the current alloy, incipient plasticity is facilitated by both homogeneous and heterogeneous dislocation nucleation mechanisms. Homogeneous dislocation nucleation occurs at higher stresses in the absence of any precursors. In contrast, heterogeneous dislocation nucleation is initiated when the probed volume contains precursors.
5. The activation volume exhibits minor variations with orientation and loading rate; however, it consistently falls within the same order of magnitude, approximately equal to one atomic volume. Upon comparison, the obtained activation volume is higher than that of pure metals and lower than that of equiatomic CoCrFeMnNi MPEA. This confirms that the incipient plasticity mechanism in FCC MPEAs differs from that in pure metals. Furthermore, the activation volume in the CoCrFeMnNi system is affected by the content of different-sized atomic species, which is known to alter SFE and energy landscapes.

ACKNOWLEDGMENTS

AC gratefully acknowledges financial support from the Indian Institute of Science, Bengaluru, for providing a start-up research grant and the Science and Engineering Research Board, Department of Science and Technology (DST-SERB, Project code: SERB/F/5812/2022-2023), Government of India. The authors thank Mr R J Vikram, Mr Tejanath Reddy, and Mr Manu Mathai for their generous help in material processing, EBSD, and APT investigations, respectively. CK and AC also recognize the Advanced Facility for Microscopy and Microanalysis (AFMM) at IISc, Bengaluru, for providing access to the characterization facilities.

CONFLICT OF INTEREST

The authors declare that they have no conflict of interest.

DATA AVAILABILITY

The data that support the findings of this study are available from the corresponding author upon reasonable request.

REFERENCES

1. D.B. Miracle and O.N. Senkov: *Acta Mater.*, 2017, vol. 122, pp. 448–511.
2. E.P. George, W.A. Curtin, and C.C. Tasan: *Acta Mater.*, 2020, vol. 188, pp. 435–74.
3. E.P. George, D. Raabe, and R.O. Ritchie: *Nat. Rev. Mater.*, 2019, vol. 4, pp. 515–34.
4. F. Otto, A. Dlouhý, Ch. Somsen, H. Bei, G. Eggeler, and E.P. George: *Acta Mater.*, 2013, vol. 61, pp. 5743–55.
5. G. Laplanche, J. Bonneville, C. Varvenne, W.A. Curtin, and E.P. George: *Acta Mater.*, 2018, vol. 143, pp. 257–64.
6. K. Lu, A. Chauhan, D. Litvinov, A.S. Tirunilai, J. Freudenberger, A. Kauffmann, M. Heilmaier, and J. Aktaa: *J. Mater. Sci. Technol.*, 2022, vol. 100, pp. 237–45.
7. B. Cantor, I.T.H. Chang, P. Knight, and A.J.B. Vincent: *Mater. Sci. Eng. A*, 2004, vol. 375–377, pp. 213–18.
8. C.-J. Tong, Y.-L. Chen, J.-W. Yeh, S.-J. Lin, S.-K. Chen, T.-T. Shun, C.-H. Tsau, and S.-Y. Chang: *Metall. Mater. Trans. A*, 2005, vol. 36A, pp. 881–93.
9. C. Wagner, A. Ferrari, J. Schreuer, J.-P. Couzinié, Y. Ikeda, F. Körmann, G. Eggeler, E.P. George, and G. Laplanche: *Acta Mater.*, 2022, vol. 227, 117693.
10. N.L. Okamoto, S. Fujimoto, Y. Kambara, M. Kawamura, Z.M.T. Chen, H. Matsunoshita, K. Tanaka, H. Inui, and E.P. George: *Sci. Rep.*, 2016, vol. 6, p. 35863.
11. C. Varvenne, A. Luque, and W.A. Curtin: *Acta Mater.*, 2016, vol. 118, pp. 164–76.
12. K. Lu, A. Chauhan, A.S. Tirunilai, J. Freudenberger, A. Kauffmann, M. Heilmaier, and J. Aktaa: *Acta Mater.*, 2021, vol. 215, 117089.
13. K. Lu, A. Chauhan, M. Walter, A.S. Tirunilai, M. Schneider, G. Laplanche, J. Freudenberger, A. Kauffmann, M. Heilmaier, and J. Aktaa: *Scr. Mater.*, 2021, vol. 194, 113667.
14. S. Sisodia, M. Rajkowski, G. Laplanche, and A. Chauhan: *Int. J. Fatigue*, 2023, vol. 174, 107723.
15. A.C. Lund, A.M. Hodge, and C.A. Schuh: *Appl. Phys. Lett.*, 2004, vol. 85, pp. 1362–64.
16. D. Wu and T.G. Nieh: *Mater. Sci. Eng. A*, 2014, vol. 609, pp. 110–15.
17. H. Jiang, Y. Lu, X. An, J. Qin, T. Xie, F. Jin, S. Zhou, W. Li, S. Long, and Y. Yi: *Mater. Sci. Eng. A*, 2023, vol. 866, p. 144651.
18. K. Gan, D. Yan, S. Zhu, and Z. Li: *Acta Mater.*, 2021, vol. 206, p. 116633. https://doi.org/10.1016/j.actamat.2021.116633.
19. D. Wu, J.R. Morris, and T.G. Nieh: *Scr. Mater.*, 2015, vol. 94, pp. 52–55.
20. S. Shim, H. Bei, E.P. George, and G.M. Pharr: *Scr. Mater.*, 2008, vol. 59, pp. 1095–98.
21. T.-H. Ahn, C.-S. Oh, D.H. Kim, K.H. Oh, H. Bei, E.P. George, and H.N. Han: *Scr. Mater.*, 2010, vol. 63, pp. 540–43.

22. M. Tomokazu and I. Yasufumi: *Eng. Fract. Mech.*, 1977, vol. 9, pp. 17–24.
23. W.W. Gerberich, J.C. Nelson, E.T. Lilleodden, P. Anderson, and J.T. Wyrobek: *Acta Mater.*, 1996, vol. 44, pp. 3585–98.
24. D.F. Bahr, D.E. Kramer, and W.W. Gerberich: *Acta Mater.*, 1998, vol. 46, pp. 3605–17.
25. E.B. Tadmor, R. Miller, R. Phillips, and M. Ortiz: *J. Mater. Res.*, 1999, vol. 14, pp. 2233–50.
26. J.K. Mason, A.C. Lund, and C.A. Schuh: *Phys. Rev. B Condens. Matter Mater. Phys.*, 2006, https://doi.org/10.1103/PhysRevB.73.054102.
27. C.A. Schuh, J.K. Mason, and A.C. Lund: *Nat. Mater.*, 2005, vol. 4, pp. 617–21.
28. H. Yang, J. Xiao, Z. Yao, X. Zhang, F. Younus, R. Melnik, and B. Wen: *Diam. Relat. Mater.*, 2018, vol. 88, pp. 110–17.
29. T. Zhu, J. Li, A. Samanta, A. Leach, and K. Gall: *Phys. Rev. Lett.*, 2008, vol. 100, 025502.
30. C. Zhu, Z.P. Lu, and T.G. Nieh: *Acta Mater.*, 2013, vol. 61, pp. 2993–3001.
31. Y. Zhao, J.-M. Park, J. Jang, and U. Ramamurty: *Acta Mater.*, 2021, vol. 202, pp. 124–34.
32. J. Xiao, N. Wu, O. Ojo, and C. Deng: *Materialia (Oxf)*, 2020, https://doi.org/10.1016/j.mtla.2020.100749.
33. M. Zhang, Q. Yu, C. Frey, F. Walsh, M.I. Payne, P. Kumar, D. Liu, T.M. Pollock, M.D. Asta, R.O. Ritchie, and A.M. Minor: *Acta Mater.*, 2022, vol. 241, 118380.
34. S. Mridha, M. Sadeghilaridjani, and S. Mukherjee: *Metals (Basel)*, 2019, https://doi.org/10.3390/met9020263.
35. Q. Zeng, K. Gan, F. Chen, D. Wang, and S. Zeng: *J. Mater. Sci. Technol.*, 2022, vol. 112, pp. 212–21.
36. S.-P. Wang and J. Xu: *J. Mater. Sci. Technol.*, 2019, vol. 35, pp. 812–16.
37. X.K. Zhang, J.C. Huang, P.H. Lin, W.S. Chuang, T.Y. Liu, Y.C. Wu, Y.C. Liao, and J.S.C. Jang: *Mater. Sci. Eng. A*, 2020, https://doi.org/10.1016/j.msea.2020.138969.
38. Y.X. Ye, Z.P. Lu, and T.G. Nieh: *Scr. Mater.*, 2017, vol. 130, pp. 64–68.
39. A.J. Zaddach, C. Niu, C.C. Koch, and D.L. Irving: *JOM*, 2013, vol. 65, pp. 1780–89.
40. C. Wagner and G. Laplanche: *Acta Mater.*, 2023, vol. 244, 118541.
41. S.F. Liu, Y. Wu, H.T. Wang, J.Y. He, J.B. Liu, C.X. Chen, X.J. Liu, H. Wang, and Z.P. Lu: *Intermetallics (Barking)*, 2018, vol. 93, pp. 269–73.
42. J. Li and C. Kirchlechner: *Mater. Charact.*, 2020, vol. 161, 110136.
43. Hertz H: MacMillan.
44. S. Pathak, J.L. Riesterer, S.R. Kalidindi, and J. Michler: *Appl. Phys. Lett.*, 2014, vol. 105, 161913.
45. F. Pöhl: *Sci. Rep.*, 2019, vol. 9, p. 15350.
46. K.L. Johnson: *Contact Mechanics*, Cambridge University Press, Cambridge, 1985.
47. A.C. Fischer-Cripps: *Introduction to Contact Mechanics*, Springer, Boston, 2007.
48. J.D. Kiely and J.E. Houston: *Phys. Rev. B*, 1998, vol. 57, pp. 12588–94.
49. S.G. Corcoran, R.J. Colton, E.T. Lilleodden, and W.W. Gerberich: *Phys. Rev. B*, 1997, vol. 55, pp. R16057-60.
50. S.A. Syed Asif and J.B. Pethica: *Philos. Mag. A*, 1997, vol. 76, pp. 1105–18.
51. A.H. Cottrell and D.L. Dexter: *Am. J. Phys.*, 1954, vol. 22, pp. 242–43.
52. S. Ogata, J. Li, N. Hirosaki, Y. Shibutani, and S. Yip: *Phys. Rev. B*, 2004, vol. 70, 104104.
53. N.L. Okamoto, K. Yuge, K. Tanaka, H. Inui, and E.P. George: *AIP Adv.*, 2016, vol. 6, 125008.
54. B. Yin, S. Yoshida, N. Tsuji, and W.A. Curtin: *Nat. Commun.*, 2020, vol. 11, p. 2507.
55. Y. Sato, S. Shinzato, T. Ohmura, and S. Ogata: *Int. J. Plast.*, 2019, vol. 121, pp. 280–92.
56. X. Zhang, P. Lin, and J.C. Huang: *J. Market. Res.*, 2020, vol. 9, pp. 8136–47.
57. G.K. Williamson and R.E. Smallman: *Philos. Mag.*, 1956, vol. 1, pp. 34–46.
58. T. Chen, L. Tan, Z. Lu, and H. Xu: *Acta Mater.*, 2017, vol. 138, pp. 83–91.
59. C.L. Kelchner, S.J. Plimpton, and J.C. Hamilton: *Phys. Rev. B*, 1998, vol. 58, pp. 11085–88.
60. G. Ziegenhain, H.M. Urbassek, and A. Hartmaier: *J. Appl. Phys.*, 2010, vol. 107, 061807.
61. G. Xu and A.S. Argon: *Philos. Mag. Lett.*, 2000, vol. 80, pp. 605–11.
62. M.J. Zehetbauer, J. Kohout, E. Schafler, F. Sachslehner, and A. Dubravina: *J. Alloys Compds.*, 2004, vol. 378, pp. 329–34.
63. L. Zuo, A.H.W. Ngan, and G.P. Zheng: *Phys. Rev. Lett.*, 2005, vol. 94, 095501.
64. P.C. Wo, L. Zuo, and A.H.W. Ngan: *J. Mater. Res.*, 2005, vol. 20, pp. 489–95.
65. J.H. Perepezko, S.D. Imhoff, M.-W. Chen, J.-Q. Wang, and S. Gonzalez: *Proc. Natl. Acad. Sci.*, 2014, vol. 111, pp. 3938–42.
66. S. Nag, R.L. Narayan, J. Jang, C. Mukhopadhyay, and U. Ramamurty: *Scr Mater.*, 2020, vol. 187, pp. 360–65.
67. M.F. Horstemeyer, M.I. Baskes, and S.J. Plimpton: *Acta Mater.*, 2001, vol. 49, pp. 4363–74.
68. I. Salehinia, S.K. Lawrence, and D.F. Bahr: *Acta Mater.*, 2013, vol. 61, pp. 1421–31.
69. T.L. Li, Y.F. Gao, H. Bei, and E.P. George: *J. Mech. Phys. Solids*, 2011, vol. 59, pp. 1147–62.
70. S.D. Kenny, D. Mulliah, C.F. Sanz-Navarro, and R. Smith: *Philos. Trans. R. Soc. A*, 2005, vol. 363, pp. 1949–59.
71. W. Wang, C.B. Jiang, and K. Lu: *Acta Mater.*, 2003, vol. 51, pp. 6169–80.
72. M.A. Tschopp, D.E. Spearot, and D.L. McDowell: *Model. Simul. Mater. Sci. Eng.*, 2007, vol. 15, pp. 693–709.
73. M.A. Tschopp and D.L. McDowell: *J. Mech. Phys. Solids*, 2008, vol. 56, pp. 1806–30.
74. J.R. Morris, H. Bei, G.M. Pharr, and E.P. George: *Phys. Rev. Lett.*, 2011, vol. 106, 165502.